Evaluation of In-Beam PET Treatment Verification in Proton Therapy With Different Reconstruction Methods

Evaluation of in-beam PET treatment verification in particle therapy with different reconstruction methods

Veronica Ferrero*, Francesco Pennazio*, Piergiorgio Cerello, Elisa Fiorina, Vincenzo Monaco, Richard Wheadon, and Magdalena Rafecas

***Abstract*—In-beam PET monitoring in particle therapy can provide early treatment quality assessment. Usually, geometrical constraints limit the scanner to open ring configurations, degrading image quality and hampering range assessment accuracy. Moreover, low production yields of positron emitters enhance image noise. To achieve the highest precision for range monitoring, it is compulsory to mitigate image noise and compensate for data truncation. The goal of this work is to study the performance of various state-of-the-art algorithms for in-beam PET image reconstruction, evaluating the impact of the system response model, and assessing the accuracy of range deviation measurement. The approaches investigated here were maximum-a-posteriori algorithms combined with total-variation and median-root priors. MLEM was used as reference. The system response was studied by comparing a Monte Carlo simulated system matrix with a single-ray tracing model. The proposed methods were tested on simulations of clinical treatment plans delivered on phantoms with air gaps of different dimension to assess the accuracy of range deviation detection. The I3PET scanner geometry was used as case study. Results show how Monte Carlo-based images lead to a more accurate range assessment, with similar performances among the used reconstruction methods. On the other hand, the addition of priors notably improves range estimation when using single-ray tracing. Our work points out the importance of carefully selecting the reconstruction approach and its implementation, since an accurate range assessment strongly depends on the accuracy of reconstruction.**

***Index Terms*—Radiation Therapy, Particle Therapy, Proton therapy, Clinical Imaging System, Positron Emission Tomography, Range Monitoring, Image Reconstruction**

I. Introduction

Ion beams used in particle therapy have a well defined, finite penetration depth, allowing at the same time a highly homogenous dose distribution in complex targets and an optimal sparing of organs at risk. However, the steep dose gradient at the end of the beam's trajectory, identified by the Bragg peak, has to be precisely localized so as not to under-dose the tumor volume or over-dose normal tissues.

Robust conservative plans are employed in the clinical practice, with (2.5 - 3.5) % $\pm$ (1 - 3) mm safety margins in the tumor volume to account for range uncertainties [1]. These can derive from a number of issues related to the patient (such as positioning, anatomical changes due to weight loss or tumor reduction during the course of the treatment, etc.), dose calculation, or Hounsfield Unit conversion methods. To better control the given treatment and reduce the safety margins, in-vivo range verification has been explored, developing the concept of secondary-radiation imaging for particle therapy applications.

The secondary particles generated from the beam interactions with the tissues include prompt photons, charged fragments, and β^+ emitting isotopes [2], [3], [4], [5], [6], [7]. The latter, in particular, have been thoroughly explored with Positron Emission Tomography (PET).

PET scanners measure the β^+ activity exploiting the co-linear 511 keV photons resulting from positron annihilation. Due to tissue composition, the most abundant β^+ emitters produced are carbon and oxygen isotopes. Alas, the resulting activity is of the order of tens of Bq/ml [8], which is at least an order of magnitude lower of that typically employed in nuclear medicine PET scans.

The low production yield and short decay time of the isotopes result in a small number of detected events - e.g., a total of $7.6 \cdot 10^4$ coincidences were measured with a dual-head PET scanner while monitoring a patient treated with a proton beam [9]. Moreover, the activity shape changes depending on the PET scan duration with respect to the treatment delivery, which introduces additional challenges as to how to perform a reliable range activity assessment. Nonetheless, recent work on particle therapy monitoring might pave the way to early treatment assessment exploiting in-beam PET scanners [10]. That is, in-beam PET scanners have the intrinsic advantage of being able to acquire the signal during the delivery of the treatment.

On the other hand, in-beam PET scanners must assure the passage of the beam and the correct patient positioning and handling. Hence, most scanners, such as the PMT-based BASTEI scanner [11], BOLPs-RGp [12], and DOPET [13], as well as the state-of-the-art INSIDE scanner [6], feature open geometries and limited angular coverage. Consequently, highly truncated projections and low statistics are some of the challenges in-beam PET must address.

The limited angular coverage of open geometries usually leads to high image noise and undesirable artefacts when using common PET reconstruction algorithms. Elongation artefacts are, for one, common in dual-head geometries, hindering an

* V. Ferrero and F. Pennazio equally contributed to this work.

V. Ferrero, P. Cerello, F. Pennazio, V. Monaco and R. Wheadon are with the INFN Sezione di Torino, Torino, Italy.

E. Fiorina is with the Centro Nazionale di Adroterapia Oncologica (CNAO), Pavia, Italy, and with the INFN Sezione di Pisa, Pisa, Italy.

M. Rafecas is with the Institute of Medical Engineering, University of Lübeck, Lübeck, Germany.

accurate estimation of the edges around the irradiated volume [14]. As the delineation of the activity volume is the most important point when doing range assessments, the development of an in-beam PET application-specific reconstruction algorithm is paramount to reduce the noise and maintain the activity edges.

To achieve the highest precision for range deviation analysis, it is compulsory to mitigate image noise and compensate for data truncation. To this aim, promising results were obtained for pencil beams and realistic treatment plans using maximum-a-posteriori (MAP) algorithms combined with total variation (TV) and median root priors (MRP) [15], [16], [17]. These studies, however, did not focus on range measurement capabilities.

MAP algorithms use a regularization parameter in the reconstruction to limit the noise, according to certain *a priori* assumptions about the data to be reconstructed, which are expressed by a weighted penalty term, here called prior. The regularization parameter is used to set the prior weight, and has to be optimized for the specific case under consideration, which is a drawback towards the general use of the algorithms.

Alternatively to MAP algorithms, early stopping of conventional maximum-likelihood expectation-maximization (MLEM) can be addressed. Previous studies have shown good results in treatment verification assessments, especially if in combination with additional post-reconstruction filtering [10], [9], [18].

The goal of this work is to study the performance of state-of-the-art algorithms for in-beam PET image reconstruction. MLEM, MAP-TV and MAP-MRP algorithms were considered. Moreover, the effect of the system response model is assessed by considering a simple single-ray tracing system matrix (SM) versus a Monte Carlo generated SM. Realistic clinical treatments are simulated and a range analysis is carried out considering the mentioned reconstruction algorithms.

II. Case Study

To enhance online monitoring performances in particle therapy, a small-scale in-beam PET scanner prototype is under development within the *In-beam PET Innovative Imaging* (I3PET) project.

The I3PET scanner will be made of 6 detector modules arranged in a 3 versus 3 partial ring configuration with 160 mm diameter, so as to permit phantom imaging with clinical hadron beams. One detector module features 4 matrices of 8 $\times$ 8 pixels (3.2 mm pitch) of segmented lutetium fine silicate (LFS) scintillating crystals. Each crystal is coupled one-to-one to Hamamatsu MPPCs, resulting in 589824 *lines of response* (LORs) within a 80 $\times$ 54.4 $\times$ 137.6 mm^3 *field of view* (FOV). A 1.6 $\times$ 1.6 $\times$ 1.6 mm^3 voxel dimension is considered. A picture of the I3PET module is reported in Fig. 1.a.

Simulation of the I3PET scanner were performed with the FLUKA Monte Carlo simulation tool [19], [20] to preliminary assess the scanner performance and are reported in [21]. The I3PET simulated scanner geometry is shown in Fig. 1.b.

For this work, the simulation of a realistic treatment plan delivered on a PMMA phantom was carried out with a biased technique already validated in a previous work [10]. Four different cases (Tab. I) were taken into consideration, so as to simulate the effects of range uncertainties: in particular, the activity distribution originating from the same treatment plan was studied on 5 $\times$ 5 $\times$ 5 cm^3 phantoms containing air gaps of 0, 2, 5, and 10 mm depth (namely case 1, case 2, case 3, case 4). The first case, corresponding to a target with no gaps, was taken as reference.

TABLE I
Simulated Treatment Plans.

	Particle	Energy (MeV)	Air gap (mm)
Case 1	Protons	43-80	0
Case 2	Protons	43-80	2
Case 3	Protons	43-80	5
Case 4	Protons	43-80	10

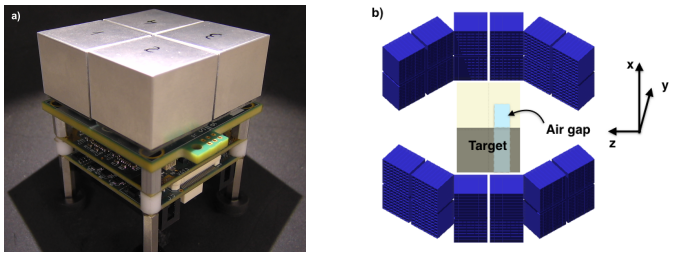

Fig. 1. (a) Picture of the I3PET detector module. (b) Geometry of the implemented simulation. The target was simulated with air gaps of different depths so as to assess the accuracy of the reconstruction algorithm in detecting range deviations. The reference system in use is shown.

A proton beam with 2 $\cdot$ 10^8 primary particles was delivered with a spread out Bragg peak (SOBP) configuration in the 43-80 MeV energy range, covering an area of 28 $\times$ 28 mm^2. The simulated statistics was evaluated according to the typical number of primary particles found in a proton treatment plan (of the order of 10^{10} primaries) and scaled to the I3PET prototype dimension. About 3 $\cdot$ 10^4 coincidences were detected for each of the simulated cases, which is comparable with the statistics observed in a clinical monitoring of a patient [9].

The simulated events were then saved in list-mode files and reconstructed with the different approaches proposed, so as to study the impact of the reconstruction algorithm and the system response model on range assessment. Five cycles per simulation were run in order to take into account statistical effects.

III. Image Reconstruction

A custom C++ based software has been developed for image reconstruction, in order to achieve both flexibility and speed optimization. Multi core CPUs are exploited by processing the list-mode coincidence file by means of BOOST-based lock-free threads. ITK libraries [22] were used for image processing.

MLEM, MAP-TV and MAP-MRP reconstruction algorithms were implemented and tested for full 3D reconstruction. In general, an iterative reconstruction algorithm can be used

for the estimation of an activity image, according to the following formula:

$$f_j^{(n+1)} = \frac{f_j^{(n)}}{\sum_i c_{ij} + \beta \cdot prior} \sum_i \frac{c_{ij}}{\sum_k c_{ik} f_k^{(n)}} \quad (1)$$

where $f_j^{(n)}$ is the intensity of the j-th pixel after iteration n. The SM elements c_{ij} represent the probability of detecting a coincidence originated within the j-th pixel by the detector pair described by the i-th LOR. Their sum over all possible LORs, $\sum_i c_{ij}$, is the system sensitivity for voxel j. Finally, the term β is the regularization parameter governing the weight given to the prior, whose form depends on the implementation, and it is zero for MLEM (i.e., β=0).

A. MLEM

The MLEM approach has been historically exploited in PET image reconstruction, and is also typically used in particle therapy PET monitoring, either with or without subsets [9], [13], [14], [17]. Ordered-subset expectation maximization (OSEM) are, in this specific application, not used, because of the little count rate statistics.

B. MAP-TV

The use of total variation was first introduced in a constrained minimization problem [23], and later used for 2D [24] and 3D [25] image reconstruction. The total variation method was found to have the capacity to smooth noise and maintain sharp edges without introducing edges artefacts. The improvement in image quality led to the suggestion of its use in particle therapy applications [15], [26].

Basically, TV uses the norm of the image gradient as the penalization criterion. Data is assumed to be locally uniform (i.e., monotonic), with pixel values approximately constant in a local neighborhood, except for at the object boundaries, where values are discontinuous. Intensity edges thus result in high gradient, preserving the discontinuity. Moreover, the TV optimization mitigates undesirable artefacts such as image elongation [15].

In this study, the MAP-TV prior was evaluated as:

$$prior = \frac{\partial}{\partial f_j} TV(f_j)|_{f_j = f_j^{(n)}} \quad (2)$$

where the cost function $TV(f_j)$ is described by

$$\begin{aligned} TV(f_j) &= \sum_{k,l,m} \sqrt{f1^2 + f2^2 + f3^2 + \epsilon} \\ f1 &= f_{k+1,l,m} - f_{k,l,m} \\ f2 &= f_{k,l+1,m} - f_{k,l,m} \\ f3 &= f_{k,l,m+1} - f_{k,l,m} \end{aligned} \quad (3)$$

with k, l, m indices of the j-th pixel in the three directions, and ϵ an additional parameter included to ensure differentiability [25]. In this case, the value $\epsilon = 10^{-6}$ was used.

A side effect of TV optimization is, though, the inability to remove the salt-and-pepper noise tipically found in PET images [27]. When the magnitude of the noise is large, it might be interpreted by the algorithm as an intensity edge and kept. An effective way to remove it is the application of a post-reconstruction median filter [28].

C. MAP-MRP

The median root prior is a well known alternative to TV to regularize image noise. That is, MAP-MRP penalizes the noise to accomodate fluctuation in the data, at the same time reducing the noise and preserving the edges [16].

To our knowledge, MAP-MRP was applied to in-beam PET proton therapy activity reconstruction first in [17], because of its robustness against missing projections.

As with the TV prior, a monotonicity of data has to be assumed. The MAP-MRP prior can be then calculated as:

$$prior = \frac{f_j^{(n)} - M_j^{(n)}}{M_j^{(n)}} \quad (4)$$

where $M_j^{(n)}$ represents the elements of an image computed as the median value of the prediction at iteration n. The image M was obtained by processing the current prediction $\sum_j f_j^{(n)}$ with a median filter of 6.4 $\times$ 6.4 $\times$ 6.4 mm^3 (4 $\times$ 4 $\times$ 4 voxels).

D. MAP-TV and MAP-MRP Parameter Optimization

The weight of the priors described by Eq. 2 and 4 for MAP-TV and MAP-MRP depends on the regularization parameter β. That is, if the implemented algorithms were to be applied for the reconstruction of a treatment in a clinical situation, in order to have an on-the-fly response the value of β should be chosen in advance.

To this purpose, the impact of β was studied on a fixed dataset with features known a priori. A FLUKA Monte Carlo simulation was conducted to produce the dataset of an evenly activated water cube of 30 $\times$ 30 $\times$ 30 mm^3 size. The same number of coincidences as those arising from the treatment plan simulation (i.e., $3 \cdot 10^4$ coincidences) was generated so as to match the working conditions of the algorithms for the case study.

The value of β was then optimized by evaluating the signal-to-noise ratio (SNR) and spill-over-ratio (SOR) of the activity cube dataset, reconstructed with MAP-TV and MAP-MRP, with both single-ray tracing and Monte Carlo generated SM. By studying SNR and SOR as a fuction of β, eventual staircase artefacts (for MAP-TV) [27], or over-smoothing of the edges (for MAP-MRP) [29], should be avoided.

SNR and SOR are calculated considering specific regions-of-interest (ROIs):

$$\begin{aligned} SNR &= \frac{\mu}{\sigma}\Big|_{ROI_1} \\ SOR &= \frac{\mu_{ROI_2}}{\mu_{ROI_1}} \end{aligned} \quad (5)$$

where μ and σ are the mean intensity and standard deviation found in the hot (cold) region ROI$_1$ (ROI$_2$). ROI$_1$ is considered as the activated cube volume, while ROI$_2$ takes into account all surrounding background. Pixels at ROIs borders were excluded in the evaluation.

E. Stopping Criterion

As the main aim of in-vivo range verification is to provide a reliable response in as little time as possible, computing time is a crucial matter. On the other hand, it has been shown how, for tomographic reconstruction, early stopping of MLEM helps reduce the noise, improving image quality [30]. Following this considerations, it was decided to consider a low number of iterations, so as to avoid noise build-up caused by low statistics and also to reduce computational time.

Five iterations were used for all algorithms considered here, as computational speed is essential for range verification. In other works it was shown that early stopping of the algorithms does not negatively affect range estimation [6], [9], [13], [18]. On the contrary, it avoids noise amplification.

F. System Response Model

To study how the accuracy of the system response model affects range verification, two approaches for the system matrix were considered.

The methods of choice represent two opposite strategies. First, a simple geometrical model based on Siddon ray-tracing [31] was calculated, considering the center of the crystals as the LOR endpoint. This method is fast and can be used for on-the-fly calculation of the matrix elements. On the other hand, as crystal penetration is not modelled, parallax errors might degrade the spatial resolution. The opposite strategy is to calculate a very accurate model using Monte Carlo simulations [32]. In this way, parallax errors can be efficiently compensated for. Simulations for the SM were carried out with FLUKA, exploiting the geometry of the I3PET scanner reproduced in Fig. 1.b.

A first order visual comparison between the two implementations was made by calculating the sensitivity of the two systems. The sensitivity images are shown in Fig. 2. As it can be seen, the simple geometrical model based on single-ray tracing (a) introduces some grid pattern artefacts which disappear when using the Monte Carlo generated SM (b). It follows that a more precise reconstruction is expected when using the latter.

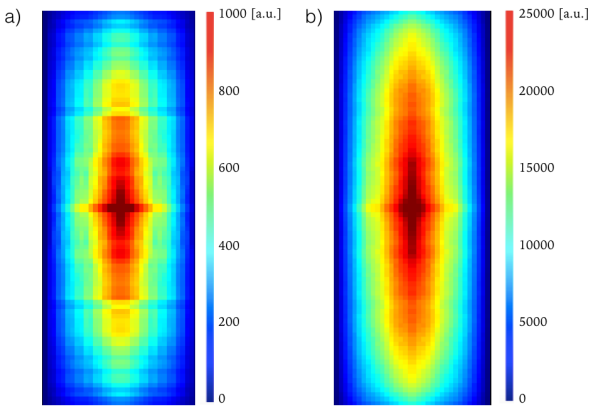

Fig. 2. Sensitivity images at comparison: single-ray tracing (a) and Monte Carlo generated (b) models. The central slice in the coronal view is shown. Images are normalized to their maximum intensity.

IV. Results

A. MAP-TV and MAP-MRP Parameter Optimization

The regularization parameter β was selected so as to maximize SNR and minimize SOR for each reconstruction method. The found values for β were equal to 0.045, 0.12 for MAP-TV, MAP-MRP images reconstructed with the single-ray tracing model, while 0.028 and 0.12 were found for the Monte Carlo model.

An example showing the activity cube reconstructed with the selected β values for MAP-TV and MAP-MRP with the single-ray tracing model is reported in Fig. 3, along with the same image reconstructed considering a non-optimal β. For the latter case, staircase artefacts can be appreciated for MAP-TV, while MAP-MRP presents an over-smoothing of the activity edges. It can also be noted how MAP-TV presents a high salt-and-pepper noise, which is treated by the algorithm as a discontinuity and thus enhanced. MAP-MRP, on the other hand, at all effects behaves as a median filter, efficiently reducing the noise.

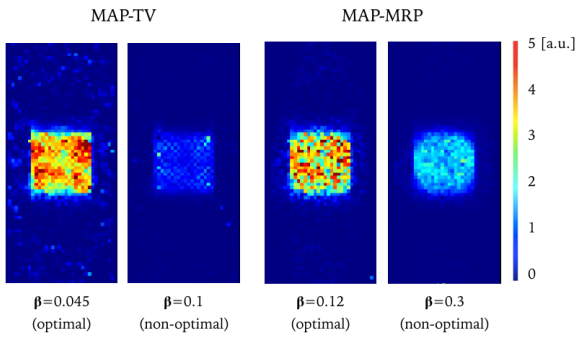

Fig. 3. Simulated $30 \times 30 \times 30$ mm^3 activity cube, reconstructed with MAP-TV and MAP-MRP methods, considering an optimal value for the regularization parameter β, and an exemplary non-optimal value. The central slice in the coronal view is shown. Intensities are normalized to the image maximum.

B. Evaluation Of Range Deviations

The simulated realistic treatment plans were reconstructed with MLEM and MAP algorithms, considering both SM implementations, for a total of 6 images per case. A sample of the reconstructed images is shown in Fig. 4, where the simulation with no air gap and air gap of 10 mm depth are shown for the reconstruction methods of choice. Images are reported without post-reconstruction filtering: it can be observed that Monte Carlo SM produces smoother images, as expected, due to the more complex description of the system model.

A total of 10 s were necessary to reconstruct images using the single-ray tracing model on-the-fly, with each iteration taking less than one second. On the other hand, using a Monte-Carlo generated SM increased the reconstruction time to about 1 min, as the SM elements generated by the FLUKA simulation needed to be stored and accessed during the reconstruction process. A multi-core system with 128GB RAM was used.

The activity distributions resulting from the addition of an air gap in the target (case 2-4) were compared to the reference

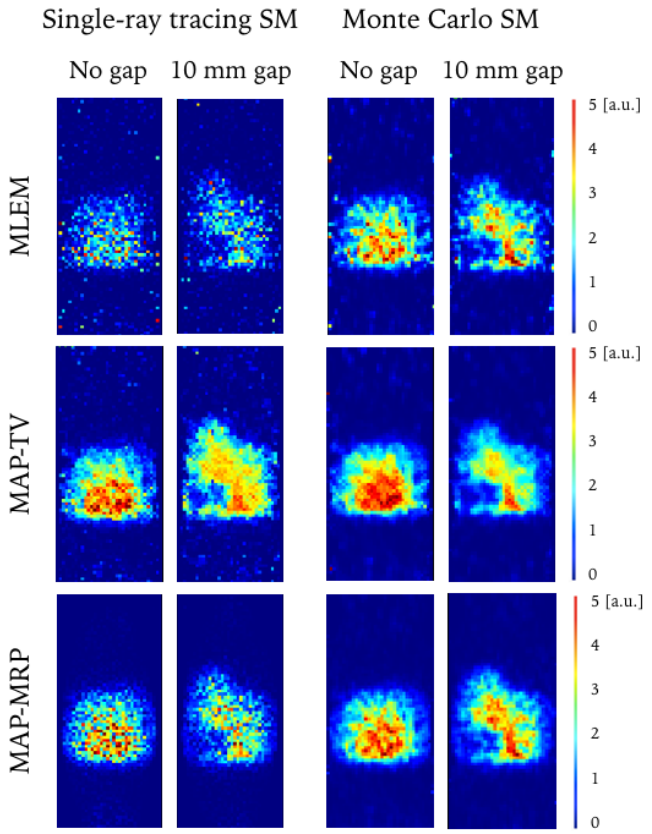

Fig. 4. Example of images reconstructed with different iterative algorithms for a treatment plan delivered on phantoms with 0, 10 mm air gap. No post-reconstruction filtering is applied to point out the differences between single-ray tracing and Monte Carlo reconstruction. The central plane in the coronal view is shown. Images are normalized to their maximum.

image (case 1). Since 5 cycles per case were run, statistics was increased by considering the non-repeated combination of images compared to each other.

The basis of the range evaluation analysis used in this work were described and validated in-vivo in [9], [10]. The analysis relays on the extraction of an iso-activity surface to discriminate the activity signal from the background, which is then used to assess the distal edge of the activity distribution along the beam direction. Range analysis considering the preferential direction of the beam were also suggested by other studies [12], [33], [34].

In the cases under consideration, the iso-activity surface was obtained by applying a threshold to exclude intensities below 10% with respect to the image maximum, followed by erosion and dilation filter in order to obtain a fully-connected distribution. Then, the distal edge of one image was subtracted from its reference, for all voxels beloging to a specific ROI (Fig. 5) in the plane normal to the beam direction. The mean value of the resulting difference distribution was then considered as the metric to describe range deviations.

To smooth out the noise caused by low statistics, MLEM images were also pre-processed with a median filter of 5 mm kernel. Despite the addition of the prior, MAP-TV and MAP-MRP images described by the single-ray tracing model also resulted too noisy to obtain a reliable iso-activity surface, so that the same pre-filtering had to be applied. Monte Carlo MAP-based images, on the other hand, already presented a smoother distribution, as shown in figure 4, thus not needing post-reconstruction filtering.

The analysis was first carried on considering only the voxels belonging to the region with the air gap (ROI (1) in figure 5). Results are summarized in Fig. 6. The range deviations are shown for the simulated treatment plan with air gaps with respect to the reconstructed reference case. The theoretical range deviation, equal to the gap dimension, is represented by the dashed line. The error bars of the calculated points were evaluated as the stardard deviation of the mean range differences, obtained by performing a non-repeated combination of images of cases 2-4 compared with the reference case 1 (i.e., the 5 images of each case were analysed with respect to the 5 images of the reference case, for a total of 25 combinations). Errors are small (below 0.5 mm) and comparable for the different methods used for the system described by the Monte Carlo SM. Similar values are obtained for images with single-ray tracing SM when considering MAP algorithms, whereas errors up to ± 2 mm are found in the MLEM case.

Results show how, for images reconstructed considering the single-ray tracing model, MLEM tends to diverge from the expected value, underestimating it for wider range deviations. MAP-TV and MAP-MRP values are, on the other hand, systematically higher, overestimating the range difference. However, results are, for all considered cases, within 1.2 mm from the expected value.

More accurate and precise range estimations are observed for images whose system response is described by the Monte Carlo generated SM. In this case, the agreement between the found range uncertainties and the expected values are within 0.6 mm. Interestingly, when using this SM the performances of the explored algorithms are very similar, even though it has to be remembered that post-reconstruction filtering was necessary for MLEM images to perform the analysis.

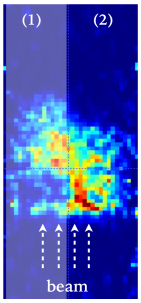

Fig. 5. Regions of interest used for the range analysis: (1) ROI including the air gap in the phantom and (2) ROI without inhomogeneities in the phantom. An exemplary image with 10 mm air gap is shown. The beam direction is also included.

In addition, the range analysis was also performed considering the region of the phantom not containig the air gap (ROI (2) in figure 5). No significant variations are expected to occur between the images in this part of the activity distribution, since no inhomogeneities are present. Results showed an agreement within 0.5 mm for all recontructed cases.

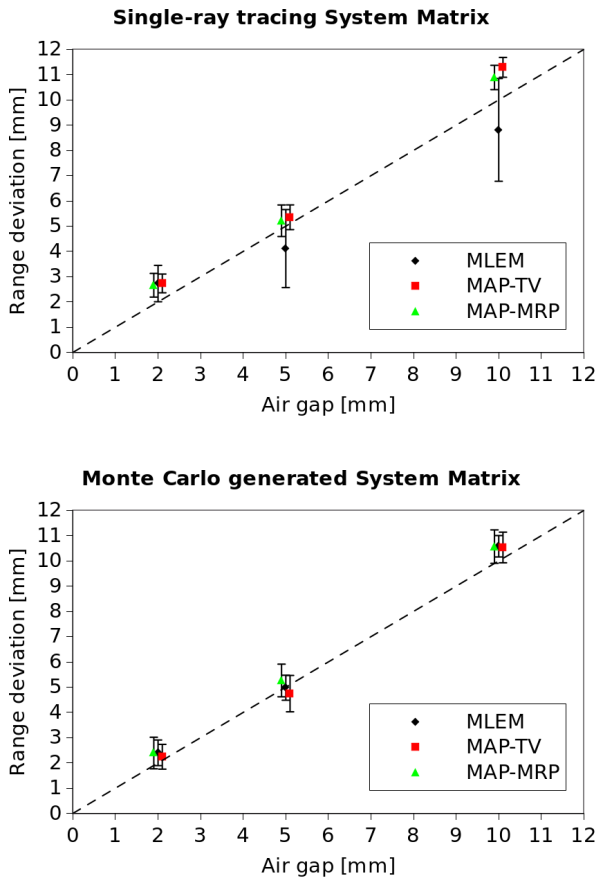

Fig. 6. Average range deviations as a function of the air gap depth. Activity images were reconstructed considering different MLEM and MAP iterative algorithms and analysed; the treatment delivered on a phantom with no gap was considered as reference. The system response was also evaluated considering a single-ray tracing SM (a) and a Monte Carlo generated SM (b) model. Error bars refer to the standard deviation of the mean range differences obtained from the analysis. The dashed line represents the expected range deviation. Data points are slightly shifted in the horizontal axis so as to help visualization.

The range analysis was also performed between images of the same simulated case (i.e., case 1 against case 1, case 2 against case 2, and so on). The found agreement was within 0.5 mm for images reconstructed with MLEM and single-ray tracing SM. On the other hand, an agreement of 0.3 mm was observed for all the other reconstruction techniques (i.e., MAP-based implementations with single-ray tracing, and all implementations with the Monte Carlo SM). These uncertainties reflect the stocastic effects of the produced activity distribution reconstructed with the implemented algorithms.

C. Conclusions

This work presents a comparison study between simulated PET images reconstructed with different methods with the aim of assessing the methods performances in view of their application in a clinical monitoring.

A simulated treatment plan delivered on phantoms containing air gaps to reproduce range uncertainties was reconstructed using different iterative algorithms. A range analysis was carried out in the region containing the air gaps to evaluate the precision of the reconstruction methods into recognising range uncertainties.

MLEM, MAP-TV and MAP-MRP approaches were explored considering a system response model described either by a simple single-ray tracing or a more complex Monte Carlo generated system matrix. A previous comparison between MAP-TV, MAP-MRP and MLEM was done in [17] for different ring configurations and time of flight (TOF) information, without however discussing the influence of the chosen methods on the activity range detection, or the system response model importance.

Out of the selected approaches, the main drawback of MLEM is, as expected, noise amplification, especially with low statistics data such as in-beam PET. The use of certain priors within the MAP algorithm can efficiently reduce noise and mitigate artefacts while preserving the edges. However, care is needed to select the adequate value of the regularization parameter, otherwise over-smoothing or staircase artefacts can distort the images.

In conventional PET, it is already known that a more accurate system model leads to higher spatial resolution. The results reported in this study show, to our knowledge for the first time, how a better system model also translates into a higher range assessment accuracy. Moreover, range estimation becomes less sensitive to the reconstruction method of choice, be it MLEM or MAP-based.

When the single-ray tracing model is considered, the addition of median post-reconstruction filtering to smooth out the noise is needed for the analysis, even for MAP algorithms. The used reconstruction methods provide a range assessment slightly divergent from the expected value, improving the result when the regularization priors are considered. Interestingly, results are very similar for MAP-TV and MAP-MRP reconstruction.

The improvement due to priors can be particularly significant when the system matrix elements have to be calculated on-the-fly (e.g., when using TOF information). The drawback is, however, that to use MAP algorithms, whose response strongly depends on the regularization parameter, β has to be defined first, and its optimal value may depend, other than the number of iteration used, also on the detected statistics.

It was also observed, by independently analysing the activity distribution of different simulation runs referring to the same case, that the stocastic effects due to the production chain of the activity distribution are reflected on the image in a slightly more significant manner when data is reconstructed with MLEM and single-ray tracing SM, with respect to the other reconstruction methods. The found agreement between images of the same case was, nonetheless, equal to or less than half millimeter. The range analysis performed considering the activity distribution in the region of the phantom without the air gap, where no significant changes are expected to occur in the activity distribution, showed results consistent with the observed stocastic effects.

The capability to provide an early assessment before the end of the treatment fraction is one of the main features of in-beam PET with respect to other PET-based particle therapy

monitoring techniques. This constrains the reconstruction and computational time.

Currently, image reconstruction takes less than one second to compute for each iteration. Multi-core CPUs were exploited to process the coincidences data in parallel, increasing the algorithm speed. However, the application of Monte Carlo SM for real-time range monitoring would presently require further work and optimization to increase the computational speed. As a compromise between the accuracy of Monte Carlo SM and the speed of single-ray tracing SM, a factorized SM including a model of the point spread function might be a good option.

In the next future we will extend our study to include the effects of the detected statistics on the choice of the β regularization parameter, with the aim of having an online feedback in both a fast and accurate manner.

In addition, the I3PET scanner prototype is now under construction, and experimental data will be used for further studies.

REFERENCES

[1] H. Paganetti, "Range uncertainties in proton therapy and the role of monte carlo simulations," *Physics in Medicine and Biology*, vol. 57, no. 11, pp. R99–R117, 2012.

[2] K. Parodi, H. Paganetti, H. A. Shih, S. Michaud, J. S. Loeffler, T. F. DeLaney, N. J. Liebsch, J. E. Munzenrider, A. J. Fischman, A. Knopf, and T. Bortfeld, "Patient study of in vivo verification of beam delivery and range, using positron emission tomography and computed tomography imaging after proton therapy," *International Journal of Radiation Oncology Biology Physics*, vol. 68, pp. 920–934, 2007.

[3] A. C. Knopf and A. Lomax, "In vivo proton range verification: a review," *Physics in Medicine and Biology*, vol. 58, p. R131R160, 2013.

[4] M. Durante and H. Paganetti, "Nuclear physics in particle therapy: a review," *Reports on Progress in Physics*, vol. 79, no. 9, 2016.

[5] S. Muraro, G. Battistoni, F. Collamati, E. De Lucia, R. Faccini, F. Ferroni, S. Fiore, P. Frallicciardi, M. Marafini, I. Mattei, S. Morganti, R. Paramatti, L. Piersanti, D. Pinci, A. Rucinski, A. Russomando, A. Sarti, A. Sciubba, E. Solfaroli-Camillocci, M. Toppi, G. Traini, C. Voena, and V. Patera, "Monitoring of hadrontherapy treatments by means of charged particle detection," *Frontiers in Oncology*, vol. 6, p. 177, 2016. [Online]. Available: https://www.frontiersin.org/article/10.3389/fonc.2016.00177

[6] M. G. Bisogni, A. Attili, G. Battistoni, N. Belcari, N. Camarlinghi, P. Cerello, S. Coli, A. Del Guerra, A. Ferrari, V. Ferrero, E. Fiorina, G. Giraudo, E. Kostara, M. Morrocchi, F. Pennazio, C. Peroni, M. A. Piliero, G. Pirrone, A. Rivetti, M. D. Rolo, V. Rosso, P. Sala, G. Sportelli, and R. Wheadon, "Inside in-beam positron emission tomography system for particle range monitoring in hadrontherapy," *Journal of Medical Imaging*, vol. 4, no. 1, p. 011005, 2017.

[7] J. Krimmer, D. Dauvergne, J. Létang, and E. Testa, "Prompt-gamma monitoring in hadrontherapy: A review," *Nuclear Instruments and Methods in Physics Research Section A: Accelerators, Spectrometers, Detectors and Associated Equipment*, 2017. [Online]. Available: https://hal.archives-ouvertes.fr/hal-01585334

[8] J. Bauer, D. Unholtz, F. Sommerer, C. Kurz, T. Haberer, K. Herfarth, T. Welzel, S. E. Combs, J. Debus, and K. Parodi, "Implementation and initial clinical experience of offline pet/ct-based verification of scanned carbon ion treatment," *Radiotherapy and Oncology*, vol. 107, no. 2, pp. 218 – 226, 2013.

[9] V. Ferrero, E. Fiorina, M. Morrocchi, F. Pennazio, G. Baroni, G. Battistoni, N. Belcari, N. Camarlinghi, M. Ciocca, A. Del Guerra, M. Donetti, S. Giordanengo, G. Giraudo, V. Patera, C. Peroni, A. Rivetti, M. D. R. Rolo, S. Rossi, V. Rosso, G. Sportelli, S. Tampellini, F. Valvo, R. Wheadon, P. Cerello, and M. G. Bisogni, "Online proton therapy monitoring: clinical test of a silicon-photodetector-based in-beam pet," *Scientific Reports*, vol. 8, no. 1, p. 4100, 2018. [Online]. Available: 10.1038/s41598-018-22325-6

[10] E. Fiorina, V. Ferrero, F. Pennazio, G. Baroni, G. Battistoni, N. Belcari, P. Cerello, N. Camarlinghi, M. Ciocca, A. D. Guerra, M. Donetti, A. Ferrari, S. Giordanengo, G. Giraudo, A. Mairani, M. Morrocchi, C. Peroni, A. Rivetti, M. D. R. Rolo, S. Rossi, V. Rosso, P. Sala, G. Sportelli, S. Tampellini, F. Valvo, R. Wheadon, and M. Bisogni, "Monte carlo simulation tool for online treatment monitoring in hadrontherapy with in-beam pet: A patient study," *Physica Medica*, 2018. [Online]. Available: http://www.sciencedirect.com/science/article/pii/

[11] W. Enghardt, K. Parodi, P. Crespo, F. Fiedler, J. Pawelke, and F. Pönisch, "Dose quantification from in-beam positron emission tomography," *Radiother Oncol.*, vol. 73, no. 2, pp. S96–98, 2004.

[12] T. Nishio, A. Miyatake, T. Ogino, K. Nakagawa, N. Saijo, and H. Esumi, "The development and clinical use of a beam on-line pet system mounted on a rotating gantry port in proton therapy," *International Journal of Radiation Oncology Biology Physics*, vol. 76, no. 1, pp. 277–286, 2010.

[13] N. Camarlinghi, G. Sportelli, G. Battistoni, N. Belcari, M. Cecchetti, G. A. P. Cirrone, G. Cuttone, S. Ferretti, A. Kraan, A. Retico, F. Romano, P. Sala, K. Straub, A. Tramontana, A. D. Guerra, and V. Rosso, "An in-beam pet system for monitoring ion-beam therapy: test on phantoms using clinical 62 mev protons," *Journal of Instrumentation*, vol. 9, no. 04, p. C04005, 2014. [Online]. Available: http://stacks.iop.org/1748-0221/9/i=04/a=C04005

[14] P. Crespo, G. Shakirin, and W. Enghardt, "On the detector arrangement for in-beam pet for hadron therapy monitoring," *Physics in Medicine and Biology*, vol. 51, no. 9, p. 2143, 2006. [Online]. Available: http://stacks.iop.org/0031-9155/51/i=9/a=002

[15] J. Cabello, I. Torres-Espallardo, J. E. Gillam, and M. Rafecas, "Pet reconstruction from truncated projections using total-variation regularization for hadron therapy monitoring," *IEEE Transactions on Nuclear Science*, vol. 60, no. 5, pp. 3364–3372, 2013.

[16] S. Alenius and U. Ruotsalainen, "Generalization of median root prior reconstruction," *IEEE Transactions on Medical Imaging*, vol. 21, no. 11, pp. 1413–1420, 2002.

[17] D. Us, K. Brzezinski, T. Buitenhuis, P. Dendooven, and U. Ruotsalainen, "Evaluation of median root prior for robust in-beam pet reconstruction," *IEEE Transactions on Radiation and Plasma Medical Sciences*, vol. 2, no. 5, pp. 490–498, 2018.

[18] F. Pennazio, G. Battistoni, M. G. Bisogni, N. Camarlinghi, A. Ferrari, V. Ferrero, E. Fiorina, M. Morrocchi, P. Sala, G. Sportelli, R. Wheadon, and P. Cerello, "Carbon ions beam therapy monitoring with the inside in-beam pet," *Physics in Medicine and Biology*, vol. 63, no. 14, p. 145018, 2018.

[19] A. Ferrari, P. Sala, A. Fasso, and J. Ranft, "Fluka: a multi-particle transport code (program version 2005)," *Tech. Rep.*, 2005.

[20] G. Battistoni, J. Bauer, T. T. Boehlen, F. Cerutti, M. P. W. Chin, R. Dos Santos Augusto, A. Ferrari, P. G. Ortega, W. Kozowska, G. Magro, A. Mairani, K. Parodi, P. R. Sala, P. Schoofs, T. Tessonnier, and V. Vlachoudis, "The fluka code: An accurate simulation tool for particle therapy," *Frontiers in Oncology*, vol. 6, p. 116, 2016.

[21] V. Ferrero, P. Cerello, E. Fiorina, V. Monaco, M. Rafecas, R. Wheadon, and F. Pennazio, "Innovation in online hadrontherapy monitoring: An in-beam pet and prompt-gamma-timing combined device," *Nuclear Inst. and Methods in Physics Research, A*, 2018.

[22] T. Yoo, M. J. Ackerman, W. E. Lorensen, W. Schroeder, V. Chalana, S. Aylward, D. Metaxas, and R. Whitaker, "Engineering and algorithm design for an image processing api: A technical report on itk - the insight toolkit," *Proc. of Medicine Meets Virtual Reality*, pp. 586–592, 2002.

[23] L. I. Rudin, S. Osher, and E. Fatemi, "Nonlinear total variation based noise removal algorithms," *Physica D: Nonlinear Phenomena*, vol. 60, no. 1, pp. 259 – 268, 1992.

[24] V. Y. Panin, G. L. Zeng, and G. T. Gullberg, "Range uncertainties in proton therapy and the role of monte carlo simulations," *IEEE Transactions on Nuclear Science*, vol. 46, no. 6, p. 2202, 1999.

[25] M. Persson, D. Bone, and H. Elmqvist, "Total variation norm for three-dimensional iterative reconstruction in limited view angle tomography," *Physics in Medicine and Biology*, vol. 46, no. 3, p. 853, 2001. [Online]. Available: http://stacks.iop.org/0031-9155/46/i=3/a=318

[26] C. Hui, D. Robertson, and S. Beddar, "3d reconstruction of scintillation light emission from proton pencil beams using limited viewing angles-a simulation study," *Physics in Medicine and Biology*, vol. 59, no. 16, p. 4477, 2014. [Online]. Available: http://stacks.iop.org/0031-9155/59/i=16/a=4477

[27] G. L. Zeng, "On few-view tomography and staircase artifacts," *IEEE Transactions on Nuclear Science*, vol. 62, no. 3, pp. 851–858, 2015.

[28] T. Huang, G. Yang, and G. Tang, "A fast two-dimensional median filtering algorithm," *IEEE Transactions on Acoustics, Speech, and Signal Processing*, vol. 27, no. 1, pp. 13–18, 1979.

[29] S. Alenius, U. Ruotsalainen, and J. Astola, "Using local median as the location of the prior distribution in iterative emission tomography image

reconstruction," in *1997 IEEE Nuclear Science Symposium Conference Record*, vol. 2, 1997, pp. 1726–1730 vol.2.

[30] T. J. Herbert, "Statistical stopping criteria for iterative maximum likelihood reconstruction of emission images," *Physics in Medicine and Biology*, vol. 35, no. 9, pp. 1221–1232, sep 1990.

[31] R. L. Siddon, "Fast calculation of the exact radiological path for a three-dimensional ct array," *Medical Physics*, vol. 12, no. 2, pp. 252–255, 1985.

[32] M. Rafecas, G. Boning, B. J. Pichler, E. Lorenz, M. Schwaiger, and S. I. Ziegler, "Effect of noise in the probability matrix used for statistical reconstruction of pet data," *IEEE Transactions on Nuclear Science*, vol. 51, no. 1, pp. 149–156, 2004.

[33] C. H. Min, X. Zhu, B. A. Winey, K. Grogg, M. Testa, G. E. Fakhri, T. R. Bortfeld, H. Paganetti, and H. A. Shih, "Clinical application of in-room positron emission tomography for in vivo treatment monitoring in proton radiation therapy," *International Journal of Radiation Oncology Biology Physics*, vol. 86, no. 1, pp. 183 – 189, 2013.

[34] K. Frey, D. Unholtz, J. Bauer, J. Debus, C. H. Min, T. Bortfeld, H. Paganetti, and K. Parodi, "Automation and uncertainty analysis of a method for in-vivo range verification in particle therapy," *Physics in Medicine and Biology*, vol. 59, no. 19, p. 5903, 2014.